AGU100 ADVANCING EARTH AND SPACE SCIENCE

JGR

Journal of Geophysical Research: Oceans

RESEARCH ARTICLE
10.1029/2018JC013830

Key Points:
- The circulation in a coastal bay was jointly controlled by the intrusion from shelf and intrinsic dynamics of the bay
- The variable shelf topography modulated the shelf circulation, and the convex isobaths enhanced its bay-ward intrusion
- The anticyclonic circulation, local wind forcing in the bay, and the baroclinic effect of the intrusive waters modulated the shelf intrusion

Supporting Information:
- Supporting Information S1

Correspondence to:
J. Gan,
magan@ust.hk

Citation:
Liu, Z., Gan, J., & Wu, X. (2018). Coupled summer circulation and dynamics between a bay and the adjacent shelf around Hong Kong: Observational and modeling studies. *Journal of Geophysical Research: Oceans*, *123*. https://doi.org/10.1029/2018JC013830

Received 6 FEB 2018
Accepted 14 AUG 2018
Accepted article online 27 AUG 2018

Coupled Summer Circulation and Dynamics Between a Bay and the Adjacent Shelf Around Hong Kong: Observational and Modeling Studies

Zhiqiang Liu[1], Jianping Gan[1,2,3], and Xiaoyan Wu[1]

[1]Division of Environment and Sustainability, The Hong Kong University of Science and Technology, Clear Water Bay, Hong Kong, [2]Department of Ocean Science and Department of Mathematics, The Hong Kong University of Science and Technology, Clear Water Bay, Hong Kong, [3]State Key Laboratory in Marine Pollution, The City University of Hong Kong, Kowloon Tong, Hong Kong

Abstract Observational and numerical modeling studies are conducted to investigate the coupled circulation between Mirs Bay to the east of Hong Kong and the adjacent shelf sea during an upwelling season. Long- and short-term observations are synthesized to characterize the circulations in the bay-shelf region. A three-dimensional-coupled bay-shelf-estuary circulation model was developed with realistic topography and forced with time-dependent wind, tides, and lateral fluxes to investigate the processes and physics in the circulation of the coupled bay-shelf regime. Based on the validated model, it was found that a strong northeastward coastal upwelling jet persisted over the shelf with highly variable topography outside the bay, and a strong upslope current occurred where the topography was sharply convex. This upslope current intruded into the bay in the lower layer (>10 m) as a cold-water stream. A horizontal anticyclonic circulation formed inside the bay with a seaward outflow in the upper layer (<10 m). Momentum and vorticity analyses showed that a southwestward along-isobath pressure gradient force over the convex isobaths off the bay intensified that bay-ward intrusion. Negative relative vorticity advection from the jet was responsible for this pressure gradient force. The horizontal anticyclonic circulation and elevation fluctuation inside the bay were determined by the interaction between the intruding shelf current and the topographic trough inside the bay, and they were also baroclinically modulated by the intrusion of denser shelf waters. Winds over Mirs Bay intensified exchange flow across its entrance but suppressed the anticyclonic circulation inside the bay.

1. Introduction

The circulation in a coastal bay is generally characterized by the wind-driven flow over the bay topography. However, this circulation often interacts in a complex manner with the adjacent shelf circulation. In this paper, the process and dynamics of a coupled bay-shelf circulation system between Mirs Bay (Hong Kong) and the neighboring shelf sea in the northeastern South China Sea (NSCS; Figure 1) is investigated, and the summer circulation, when the currents are driven by the southwesterly upwelling favorable monsoon winds (Gan, Cheung, et al., 2009), is the focus of this research.

Figure 1 shows the bottom topography of the shelves southeast of Guangdong and near Hong Kong. The waters in the study area are generally shallower than 70 m, and the isobaths extend mainly northeastward, parallel to the coast (~22.8° east; Figure 1a). The seaward convex coastline of Hong Kong features a unique coastal promontory along the Guangdong coast (Figure 1b). Mirs Bay lies northeast of this promontory and is generally shallower than 20 m. It has a bell-shaped isobath and forms a trough topography with a deep channel along the central axis of the bay. On the lee side of Hong Kong in summer, the 20- to 30-m isobaths extend northeastward toward Mirs Bay and form a topographic trough (Figure 1b). To the west of Hong Kong, the trapezoid-shaped Pearl River Estuary (PRE) penetrates northwestward from the shelf. The PRE discharges freshwaters at ~15,000 m^3/s onto the shelf and modulates the wind-driven upwelling circulation in the summer (Gan, Li, et al., 2009).

Few studies exist on the circulation in Mirs Bay and upwelling circulation in the adjacent shelf. Chau and Abesser (1958) reported that waters in the bay were not greatly affected by the prolonged eastward buoyant plume from the PRE. Both Yin (2002) and Lee et al. (2006) mentioned a shoreward invasion of oceanic deep

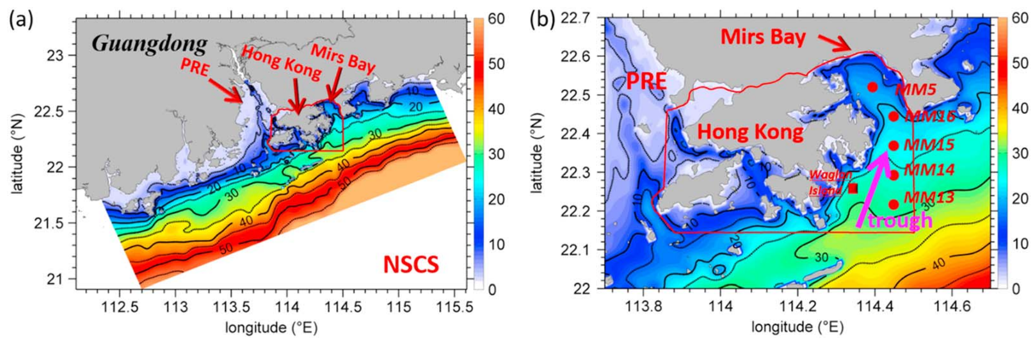

Figure 1. (a) The model domain and bathymetry (m; color contours with black contour lines); and (b) magnified view of the shelf topography near Hong Kong. MM13, MM14, MM15, MM16, and MM5 denote the Water Quality Monitoring Stations in Mirs Bay. The solid red square in (b) indicates the location of Waglan Island. PRE refers to the Pearl River Estuary. NSCS = northeastern South China Sea.

shelf waters in the lower layer of Mirs Bay's entrance. However, the characteristics of the circulation in the bay and its coupling with the intrusive shelf current have never been investigated.

Onshore intrusion of coastal waters under upwelling-favorable circumstances can be amplified on the lee side of promontories due to alongshore variations in coastal topography (Song et al., 2001; Tee et al., 1993; Weisberg et al., 2000). As the promontory naturally exists at the entrance of the bay, the intrusion of the shelf water provides external flux for the circulation in the bay. Gan and Allen (2002) found that the promontory topography usually induces a countercurrent pressure gradient force downstream of the shelf current. This pressure gradient force makes the onshore invasion of deep shelf waters much stronger than the current induced by bottom friction. Gan et al. (2013) and Liu and Gan (2014) suggested that this countercurrent pressure gradient force originates mainly from a net stress curl and the nonlinear advection of the relative vorticity in the water column.

The shoreward intrusion of deep shelf waters, which is often related to the dynamics of local cross-isobath transport, also alters the flow pattern in bays located landward of the upwelling circulation. For example, Klinck et al. (1981) found that the intrusion of deep and denser shelf water affected the surface elevation and pycnocline displacement near the entrance of a fjord and the circulation in the fjord. This research reports that the geostrophic alongshore current, forced by the southwesterly wind stress on the shelf off the fjord, is responsible for the intensified intrusion of the deep shelf waters. The impact of the shelf current on bay circulation was also found to impose a nonlocally forced current fluctuation in the Chesapeake Bay (Wang & Elliott, 1978) and the Delaware Estuary (Wong & Garvine, 1984). Observational and numerical modeling studies conducted in the Ría de Muros (northwest Spain) suggested that when upwelling-favorable winds prevailed, the upper-layered waters inside the bay were transported seaward, and an upslope shelf water was formed in the lower layer to compensate the outflow in the upper layer. This process formed a two-layer exchange flow at the bay entrance when an upwelling-favorable wind prevailed (Souto et al., 2003). The generation of this exchange flow was mainly due to wind forcing and buoyancy discharges inside the bay (Carballo et al., 2009). Moraga-Opazo et al. (2011) observed that bay-shelf interactions during an upwelling period triggered a cyclonic recirculation inside the Tongoy Bay in Chile. Most of these previous researches on bay-shelf interactions considered mainly the circulation inside bays or estuaries without adequately linking it with the shelf circulation and dynamics. The coupled forcing processes in the shelf-bay circulation as well have attracted little attention.

This study investigates the coupled bay-shelf circulation and the associated dynamics by linking the shelf circulation in the NSCS with the flow field in the Mirs Bay. The cross-isobath transport for bay-ward intrusion during an upwelling period and the bay circulation in response to local wind forcing and the intrusion are explored. We combine field observations with a numerical model to investigate the underlying dynamics. Section 2 of this paper describes the implementations of observation and the numerical model. Characteristics of the upwelling circulation and the coupled bay-shelf circulation, based on long- and short-term observations, as well as results from the numerical model are presented in section 3. The forcing mechanisms that govern the onshore intrusion over the shelf and the response of circulation in Mirs Bay are discussed in section 4. Section 5 summarizes the finding.

2. Observations and Ocean Model

2.1. The Climatological Records

Figure 2a uses a wind rose to illustrate the statistical characteristics of the wind stress in the summer (June to August), 1991–2011. We calculate the wind stress, according to Large and Pond (1981), at 10 m above the sea surface at Station MM13 off the bay entrance (Figure 1b). The wind field is obtained from the satellite-observed, cross-calibrated, multiplatform ocean surface wind velocity released by the Jet Propulsion Laboratory (JPL) of NASA.

The long-term (1991–2013) observed temperature profiles from the Marine Water Quality Monitoring Stations (Figure 1b) are analyzed to illustrate the general characteristics of ocean circulation in the Mirs Bay and the adjacent shelf sea. These stations are operated by the Environmental Protection Department of Hong Kong. The hydrographic properties at those stations were sampled by using the conductivity-temperature-depth (CTD) profiler, and the observation was conducted once in the middle of June, July, and August of each year. Their bottom depths (*hs*) and observation periods are summarized in Figure 2b. These stations were generally positioned northward over the shelf between the 20- and 30-m isobaths, and the samplings were conducted at depths of the surface ($0.0 \times hs$), middle ($0.5 \times hs$), and bottom ($1.0 \times hs$) in the water column.

Figure 2c demonstrates the long-term averaged sea surface temperature (SST) observations in Hong Kong waters during summer. These SST observations were retrieved from the daily, global, multiscale, ultrahigh resolution SST data set with 1-km resolution and provided by JPL of NASA. Figure 2d shows the summer-averaged temperature structure along the cross-shore transect extended from the shelf to the bay.

2.2. Field Observations

High-resolution field measurements of velocity, temperature, and salinity along transects in the bay are conducted from 22 to 26 July 2011 to better reveal the detailed structure of the circulation and hydrographic properties. Figure 3 illustrates the atmospheric, buoyancy, and tidal forcing conditions in June and July 2011. The time series of wind stress at 10 m above the sea surface (Figures 3a and 3b) at Station MM13 was from the JPL data set of NASA. The Pearl River discharge data (Figure 3c) were obtained from a hydrographic monitoring station in the upstream of the Pearl River. The hydrographic station is operated by the Chinese Ministry of Water Resources. The Hong Kong Observatory provided the tidal elevations measured by the tide gauge at the Waglan Island, southwest of Mirs Bay (Figure 1b).

An hourly sampling of velocities and CTD profiling at the entrance of the bay (station MBT, Figure 4a) during the cruise period were conducted, and a simultaneous mapping over the along-bay transect (*A*) and cross-bay transects (*B* to *E*) inside the bay (Figure 4a) were performed. In order to increase the spatial resolution of the sampling, we established five stations along the transects *B* to *E* and 10 stations along the longer transect *A*. A precruise numerical simulation is conducted to optimize the location and time of the mapping survey. At each station, a Seabird CTD profiler was deployed during flooding and ebbing tides to measure the vertical profiles of temperature and salinity during these periods, respectively. The temperature observations during the ebbing and flooding tides are then averaged to mitigate the variation caused by the oscillating tidal current.

2.3. Ocean Model

The Regional Ocean Modeling System (Shchepetkin & McWilliams, 2005), which has three-dimensional and time-dependent primitive equations with a free surface, was used in this study. The parameterization of vertical mixing process of the submodel is based on Mellor and Yamada (1982), which solves the 2.5-layered turbulent kinetic energy equations.

The model domain, shown in Figure 1a, extended northeastward and covered the PRE and the shelves off Guangdong in the NSCS. The study area was discretized into an Arakawa C-grid system with 1-km horizontal resolution. The bottom topography was retrieved from the navigation maps provided by the Hong Kong

10.1029/2018JC013830

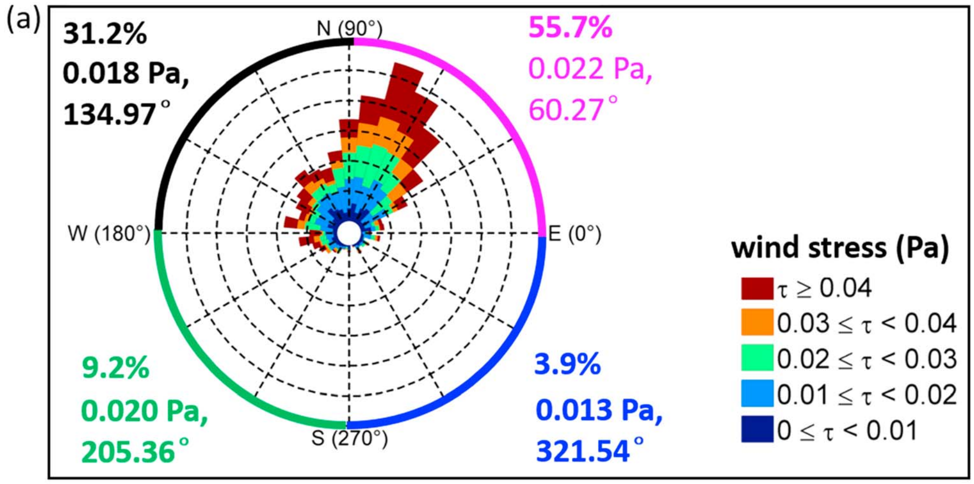

(b)

	MM13	*MM14*	*MM15*	*MM16*	*MM5*
period (year)	1991-2013	1994-2013	1994-2013	1994-2013	1991-2013
depth (m)	28	25	24	22	20

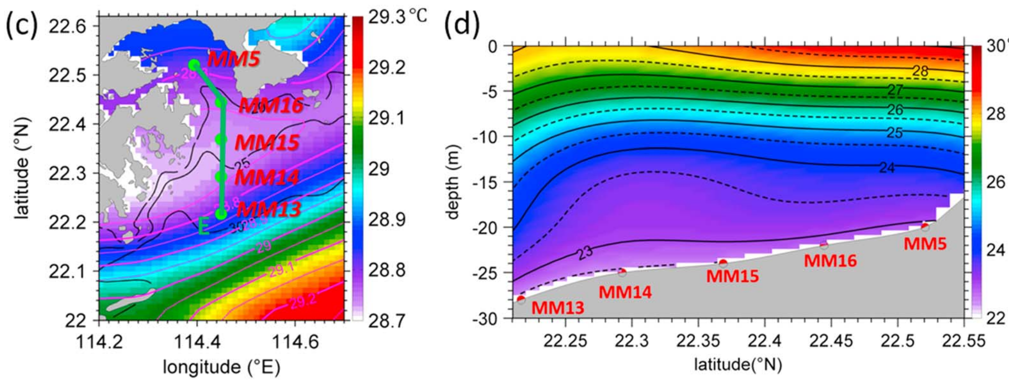

Figure 2. (a) Wind rose of summer (June–August) wind stress at station MM13 during 1991–2011; (b) water depth and hydrographic observation period at the Water Quality Monitoring Stations shown in (c). (c) Long-term-averaged (2002–2015) summer sea surface temperature (°C) for Hong Kong waters; and (d) long-term-averaged (1991–2013) summer temperature (°C) profile along the section dotted by the Water Quality Monitoring Stations.

Maritime Department and the China Maritime Safety Administration. The model had 30 vertical levels with terrain-following *s* coordinates (Song & Haidvogel, 1994) and adopted higher resolutions (<0.2 m) in both the surface and bottom boundary layers to better resolve the dynamics inside these boundary layers. A detailed description of model implementation and validation are described in Zu and Gan (2015).

The model was nested within an NSCS model with a coarser resolution (~3 km; Gan et al., 2015). This NSCS model was further downscaled from a hindcast simulation in the China Seas Multiscale Modeling System (Gan et al., 2016). This downscaling system ensured that the remote effect from the NSCS circulation during the cruise period can be well resolved.

The model was initialized with temperature and salinity on 15 June 2011 from the NSCS simulation, and the remote forcing of velocities and hydrographic variables from the NSCS model along the three open boundaries (OBs) were imposed (Figure 1a) by using the OB conditions of Gan and Allen (2005). Tidal forcing along the OBs was derived from the harmonic constants based on the Oregon State University Tidal Inversion Software (Egbert & Erofeeva, 2002), which has been validated by Zu et al. (2008), which was implemented along the OBs by an *active* Flather (1976)-type OB condition. We included eight tidal constituents, M_2, K_1,

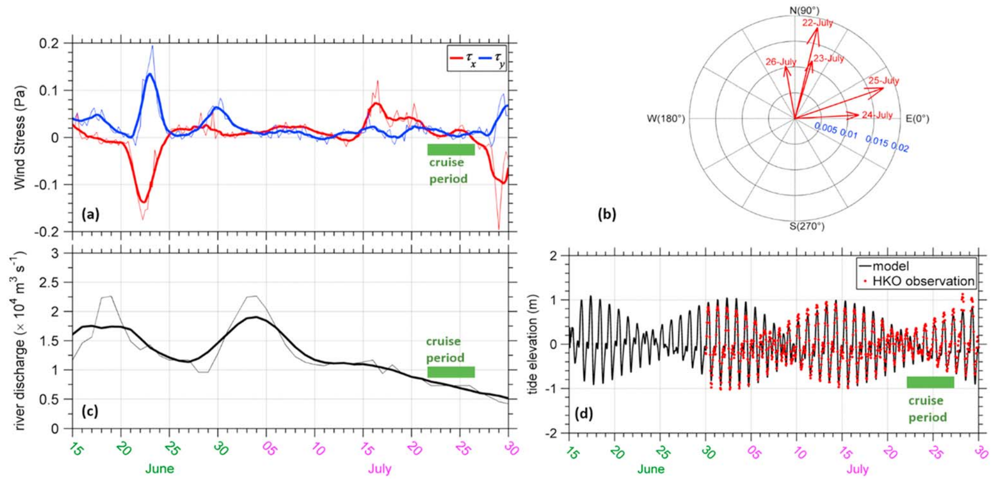

Figure 3. (a) Time series of wind stress (Pa) at station MM13 in June and July 2011; and (b) variation of wind stress (Pa) during the cruise (22–26 July 2011); (c) river discharge ($\times 10^4$ m^3/s) observed at the hydrological station at Gaoyao upstream of the Pearl River; and (d) time series of observed tidal elevation (m) at the tide gauge at Waglan Island (red dots) and the simulated tidal elevation (black line). HKO = Hong Kong Observatory.

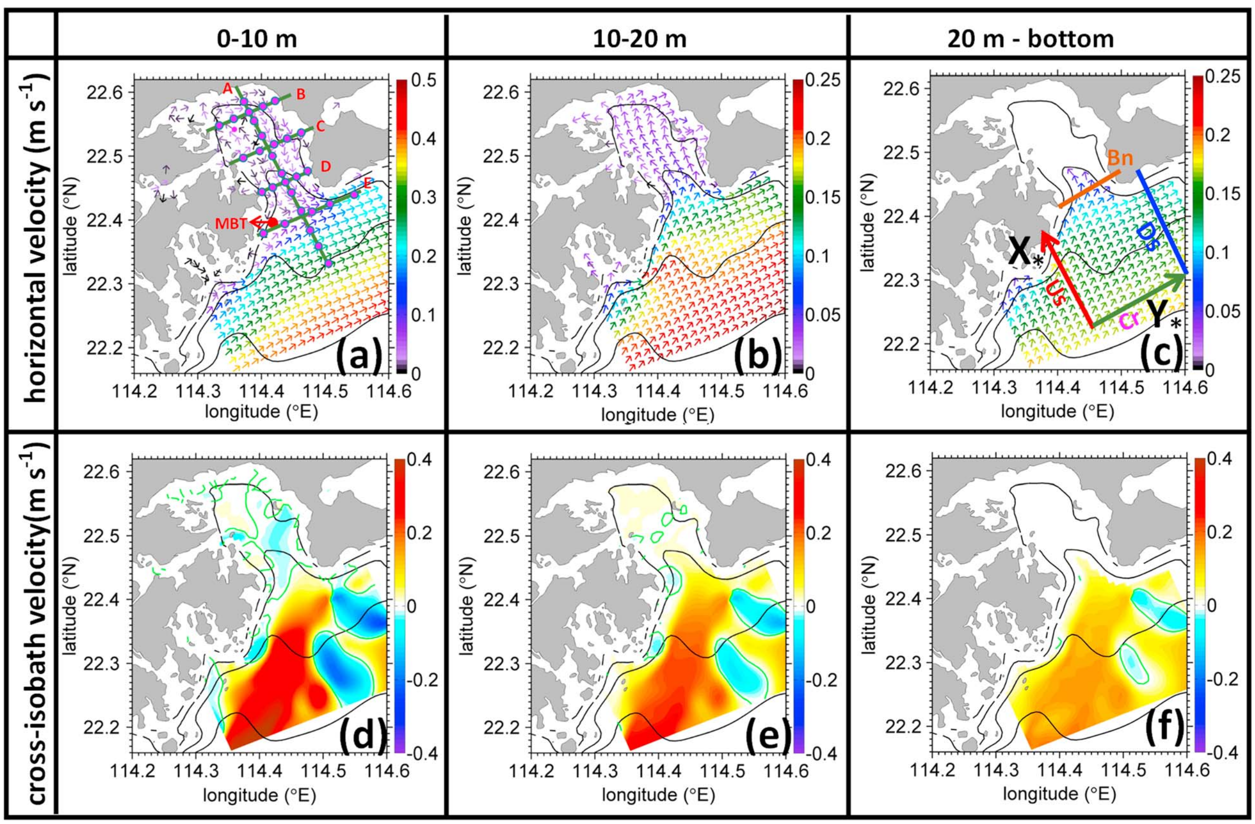

Figure 4. (a–c) The simulated horizontal velocity (m/s) vectors on the shelf neighboring Mirs Bay and averaged over the (a) upper (0–10 m), (b) intermediate (10–20 m), and (c) lower (20 m–bottom) layers. The velocity (m/s) component in the cross-isobath direction is illustrated in (d)–(f). A positive value in (d)–(f) represents a shoreward velocity component crossing the isobath. The color scale in (a) is larger than that in (b) and (c). The contour lines are the 30-, 25-, 20-, and 15-m isobaths from the shelf toward the bay. The cruise transects and time-series observations for station MBT are illustrated in (a).

S_2, O_1, N_2, P_1, K_2, and Q_1 and used Hong Kong Observatory meteorological variables observed at the weather station on Waglan Island to calculate bulk heat flux.

3. Processes of Shelf-Bay Circulation

3.1. The Climatological Hydrographic Fingerprint

A southeasterly wind directed northeastward (~60.27° east) prevailed for ~55.7% of the days for those summer months during 1991–2011 (Figure 2a). The alongshore wind stress, which blew northeastward (~22.8° east) along the isobaths/coastlines of Guangdong, was ~0.017 Pa in the summer.

A notable lower surface temperature centered on the shelf near Station MM14 off the bay was the result of intensified upwelling on the lee side of Hong Kong (Figure 2c), as a result of coastal promontory dynamics (Gan & Allen, 2002; Liu & Gan, 2014). These surface upwelling waters elongated northeastward and bypassed the entrance of Mirs Bay. However, a large amount of the cold shelf waters in the intermediate and lower layers advanced bay-ward, where the isothermals were uplifted and temperature increased progressively from the entrance toward the interior of the bay (Figure 2d).

3.2. Shelf-Bay Circulations

Figure 3 shows that southwesterly winds prevailed in June and July 2011. The along- and cross-shore components of the wind stress were ~0.010 and ~0.007 Pa, respectively. The discharge rate of the Pearl River decreased in June 2011. The observed mean runoff during the cruise period was ~7,400 m^3/s, and the cruise took place on 22–26 July 2011 during a neap tide.

The simulated circulation, averaged over the cruise period, in the upper (0–10 m), intermediate (10–20 m), and lower (20 m–bottom) layers is shown in Figures 4a–4c. The colors of the arrow indicate magnitude of the shelf current. The cross-shore component of the shelf velocity, perpendicular to the isobaths, is shown in Figures 4d–4f to illustrate the intensity of the cross-shore intrusion, and a positive value represents a shoreward current.

An extensive northeastward-flowing upwelling jet characterized the shelf circulation off the bay throughout the entire water column (Figures 4a–4c). The core of this jet positioned over the 30-m isobath largely because of the effect of the buoyant plume from the PRE (Gan, Li, et al., 2009). The main stream of the jet bypassed the entrance of Mirs Bay and flowed northeastward without entering the bay in the upper layer. The intrusion occurred in the intermediate and lower layers (Figures 4b and 4c), similar to observations in Figure 2d.

Inside the Mirs Bay, the current rotated in an anticyclonic direction in the upper layer. The offshore outflow in the upper layer (Figure 4a) and an extensive onshore intrusion of the deep shelf waters below formed a two-layer exchange (Figures 4b and 4c). The intrusive shelf water was originated from the intensified bay-ward cross-isobath velocity (>0 m/s) over the trough offshore at ~22.2°N (Figures 4d–4f). This onshore transport occurred in the entire water column, implying the strong influence of local topography.

The three-dimensional characteristics of shelf circulation and the exchange flow are shown by the along- and cross-shore velocity transects over the shelf upstream (*Us* in Figure 4c) and downstream (*Ds* in Figure 4c) of Mirs Bay and along transects *A* and *E* inside the bay in Figure 5, respectively. The alongshore velocity showed that the northeastward coastal jet occupied mainly the upper 20 m of the water column and maintained its intensity from the upstream to the downstream along the bay entrance. In response to the alongshore jet, a strong shoreward transport across the entrance of Mirs Bay (Figures 5e–5g) was generated. A much larger shoreward velocity occurred along line *Us* as a result of the intensified shoreward cross-isobath transport over the topographic trough. This intensified intrusion was also clearly shown by the velocity normal to transect *E* (Figure 5h).

At the entrance of the Mirs Bay (transect *E*, Figure 5h), we noticed that there was a two-layer exchange flow, which is consistent with observations. This two-layer exchange flow also characterizes the circulation in Mirs Bay, with seaward export in the upper layer and bay-ward invasion in the lower layer over transect *A* (Figure 5f).

Both the observed and simulated time series of velocity fields at the MBT station (Figure 4a) suggest that the two-layer flow existed at the entrance of Mirs Bay, where there was a seaward outflow of bay waters above 10 m and a persistent bay-ward current beneath it (Figures 6a–6d). This finding showed that, although tidal

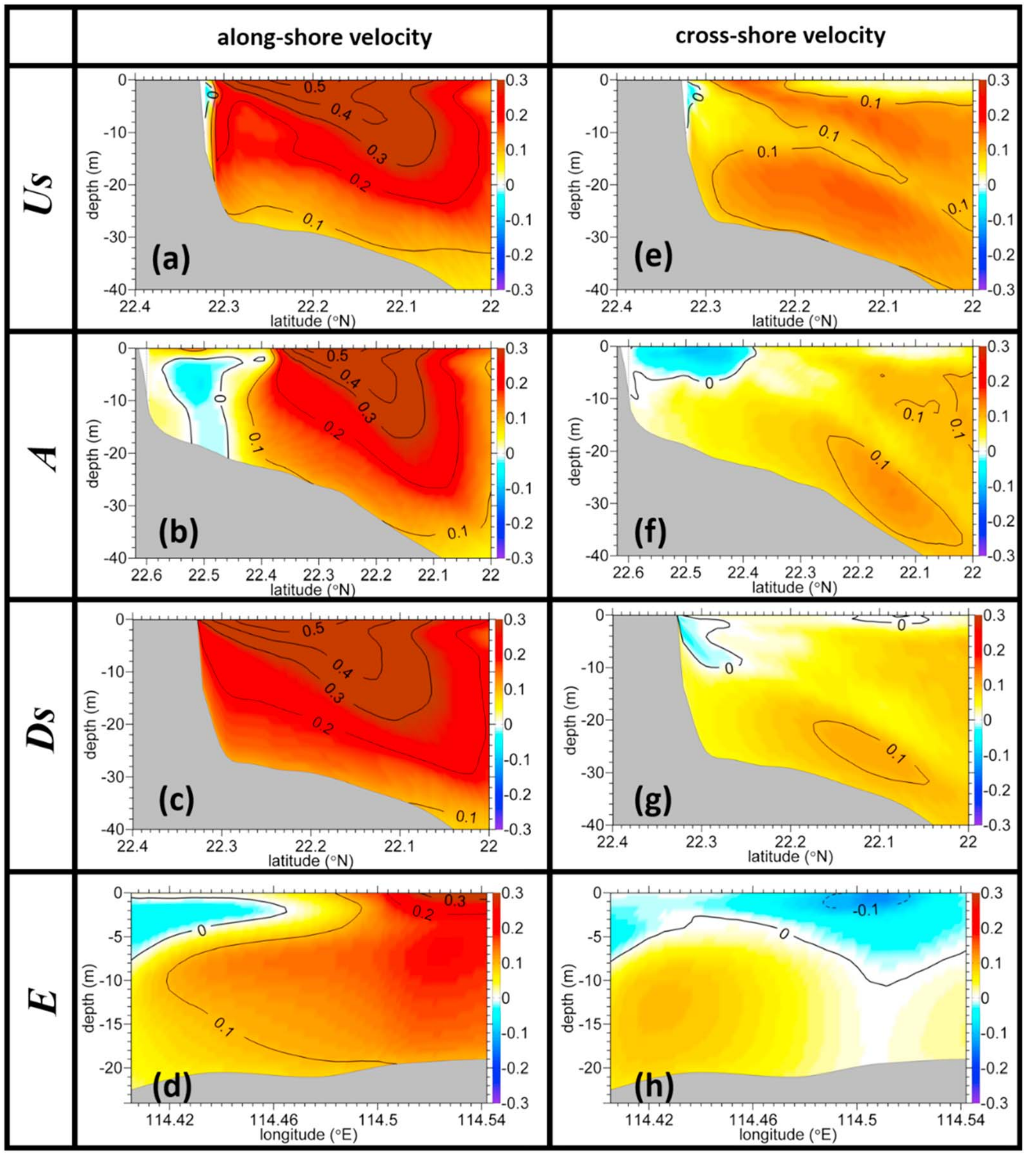

Figure 5. (a–d) The simulated alongshore velocity (m/s) profiles over the transects (a) upstream (transect *Us*) and (c) downstream (transect *Ds*) of Mirs Bay, as well as over the transects (b) *A* and (d) *E* inside the bay. (e)–(h) illustrate the cross-shore velocity (m/s) profiles over these transects. A positive value represents a northeastward flow in (a)–(d) and a northwestward flow in (e)–(h). The locations of the transects are shown in Figures 4a and 4c.

forcing provided the strongest periodic variation (Figure 3d), the dominant shelf circulation and the exchange flow were mainly determined by the subtidal dynamics.

3.3. Hydrographic Response to Circulation

Both the observed and the simulated SST anomalies (calculated by subtracting the horizontal mean SST from the SST observations) showed that a cold-water stream elongated along the shelf off the entrance of Mirs Bay (Figures 7a and 7d). This surface cold-water stream persisted in the shelf segment of transect *A* during the cruise period (Figures 7b and 7e), when the southwesterly monsoon prevailed. The cold water extended northeastward following local isobaths without clear bay-ward intrusion. At the bottom, however, the deep cold shelf water intruded into the bay, as shown by the bottom temperature anomaly calculated from both the field data and the numerical simulation (Figures 7c and 7f). These detailed features are consistent with the observed upwelling characteristics in section 3.1.

10.1029/2018JC013830

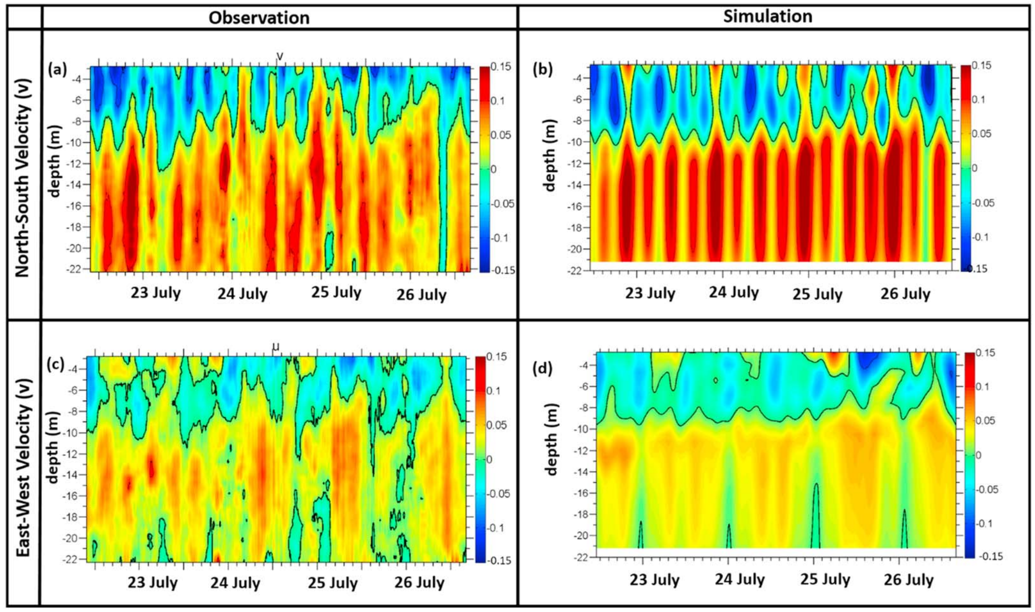

Figure 6. Observed (a) north-south and (c) east-west velocity profiles (ms^{-1}) at the MBT station (Figure 4a) during the cruise. The simulated time series of velocity profiles at the MBT station for the north-south and east-west directions are illustrated in (b) and (d), respectively.

The temperature field in the upper, intermediate, and lower layers (Figures 7g–7i) suggests that both the surface cold-water stream and the strengthened onshore intruding deep shelf waters originated from the intensified upslope transport over the northeastward-oriented trough off the bay entrance. The bay-ward cold tongue below 10 m was mainly guided by the trough isobaths on the lee side of the Hong Kong Island and farther offshore. These trough isobaths, together with the effect of the coastal promontory, intensified the bay-ward intrusion.

In response to the two-layer exchange flow (Figures 6a and 6b), the time series of temperature exhibited a prominent-layered structure. The deep cold water constantly flowed shoreward in the lower layer, while a diurnal heating-cooling cycle, which is mainly exerted by the diurnal variation of atmospheric heat flux over the sea surface, existed in the upper layer (Figures 8a and 8b). The upper and intermediate layers at the bay entrance were well separated at 10 m. A similar case appeared along the transect *A*, which extended southeastward from Mirs Bay to the shelf (Figures 8c and 8d). The cold shelf waters below 10 m advanced shoreward and entered Mirs Bay. Apparently, this observed flow exchange between the shelf and bay prevailed in the summer, as also shown in section 3.1.

Inside the bay, the temperature profiles for transect *E* (Figures 8e and 8f) showed that there was a cold-water dome at the entrance of the bay, where the 22 °C isotherm had risen. This dome was associated with the core of the upslope cold-water intrusion from the shelf (Figures 4d–4f) and coincided with bay-ward protruded trough isobaths.

Warm water inside the bay flowed mainly southeastward in the upper layer. Compared with transect *E*, the bay-ward intrusion of deep shelf water is extensively diminished along transect *D* (Figures 8g and 8h), as shown by the subducted 22 °C isotherm.

4. Physics of the Coupled Bay-Shelf Circulation

Observational and modeling studies have shown that the coupled bay-shelf circulation, in which the intensified upslope deep shelf current followed the trough isobaths, intruded into Mirs Bay and formed an anticyclonic bay circulation. In this section, the underlying physics that govern this coupled bay-shelf circulation will be investigated. Sensitivity experiments are conducted to distinguish the local and remote forcings for

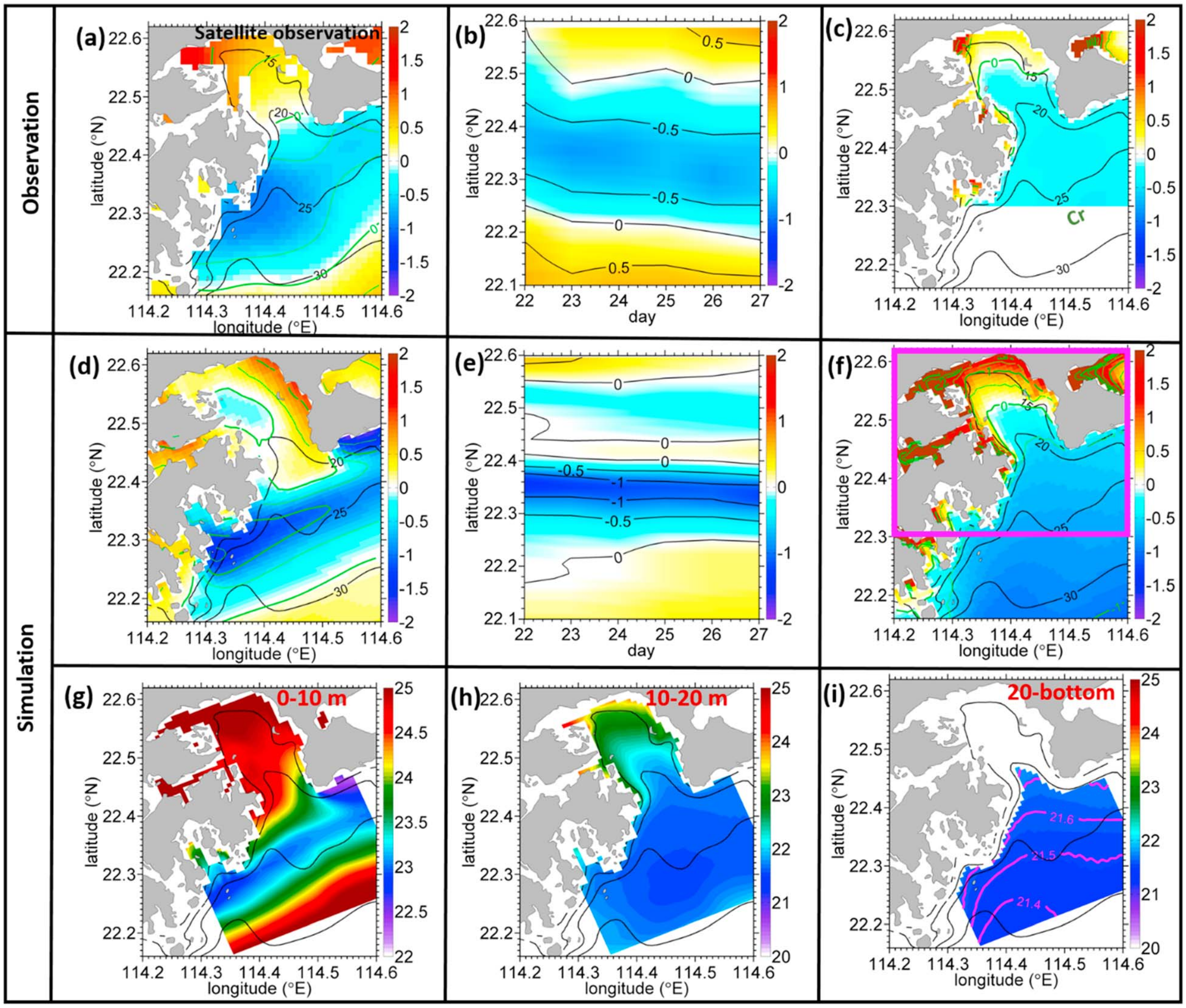

Figure 7. (a) Averaged SST anomaly (SSTA, °C) from satellite remote sensing; (b) time series of SSTA (°C) along transect *A*; (c) field measurement of bottom temperature during the cruise (22–26 July 2011). The corresponding simulated SSTA (°C), time series of SSTA (°C) along transect *A*, and bottom temperature (°C) distribution during the cruise are exhibited in (d) to (f), respectively. Temperature (°C) averaged for the cruise period and in the upper (0–10 m), intermediate (10–20 m), and lower (20–bottom) layers on the shelf neighboring Mirs Bay is shown in (g)–(i). The color scale in (g) is smaller than that in (h) and (i). SST = sea surface temperature.

the bay circulation, as well as the role of the trough isobaths over the shelf on the bay-ward transport on the lee side of Hong Kong. The case, whose results are presented in the section 3, is defined as standard case.

4.1. Characteristics of the Bay Circulation

The depth-averaged relative vorticity (ξ) over the shelf and inside Mirs Bay is calculated and decomposed into shear ($\xi_s = -\frac{\partial V}{\partial n}$) and curvature ($\xi_c = \frac{V}{R_s}$) components (Figures 9a and 9b) in the natural coordinate (n, s) to better reveal the bay-shelf circulation shown in Figures 4a–4c. V is magnitude of the velocity field, and R_s denotes the radius of curvature of the streamline. Figure 10 shows the time series of alongshore (oriented ~22.8° east) upwelling wind stress at station MM13, the time series of surface elevation (η), and the time series of ξ averaged over a bay area (purple curve in Figure 9a). Figure 10 also displays the net transport and exchange flow across the bay entrance over section *Bn* (Figure 4c) in July 2011. A 3-day low-pass filter is applied to these time series to better identify their relationships.

Figures 9a and 9b clearly show that the circulation in Mirs Bay is characterized by an anticyclonic circulation attributed to both ξ_s and ξ_c. This anticyclonic circulation weakened over the trough isobaths at the bay

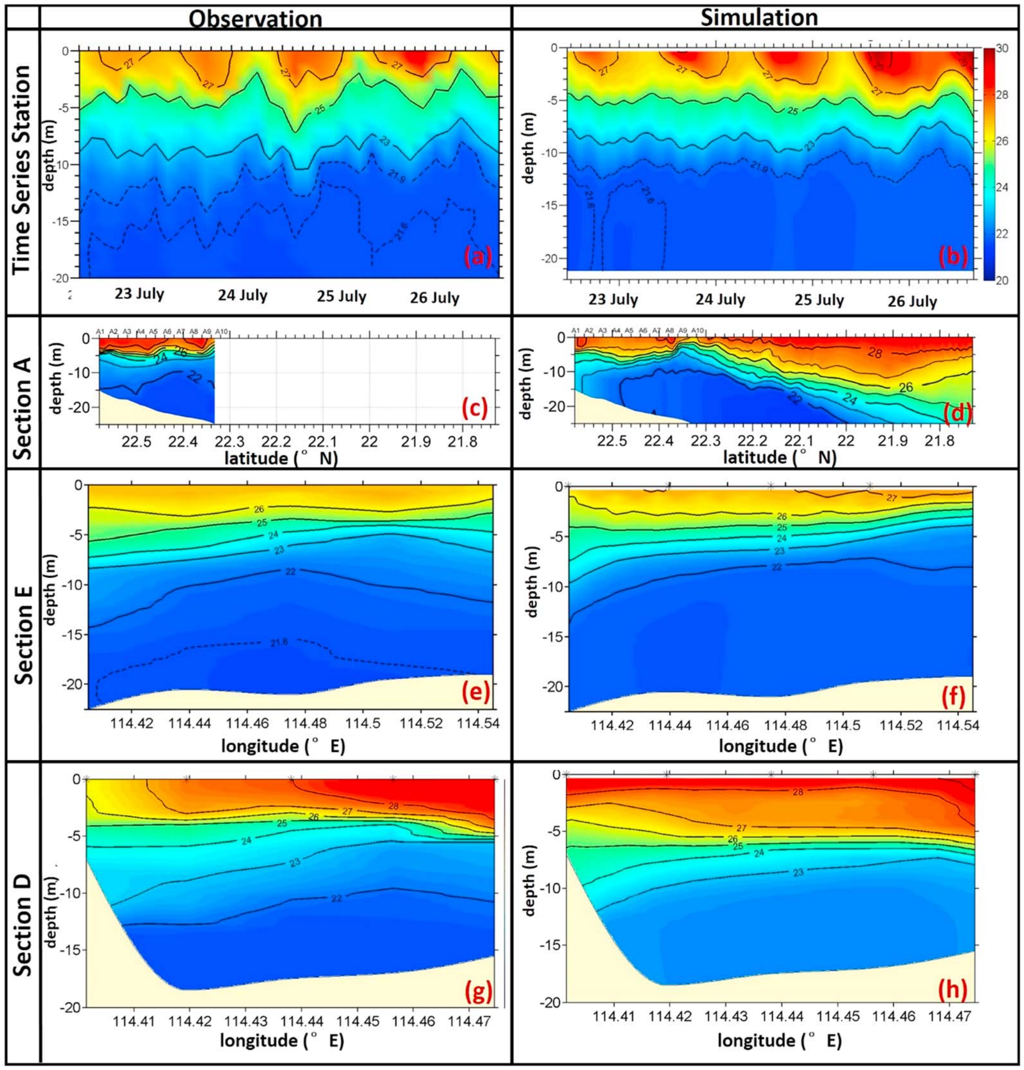

Figure 8. Observed (left) and simulated (right) time series of 3-hourly temperature (°C; a, b) at station MBT and profiles along (c, d) transect *A*, (e, f) transect *E*, and (g, h) transect *D*. The cruise stations and transects are shown in Figure 4a.

entrance, where ξ_c was positive. The denser shelf waters, guided by the trough isobaths, intruded into the Mirs Bay (also see Figure 4b). Over the shelf on the lee side of Hong Kong, a positive ξ_s on the shoreside of the shelf current and a negative ξ_c due to the eastward flow over the local isobaths were observed (also see Figure 4a).

The anticyclonic bay circulation was jointly determined by local and remote forcings. The alongshore wind stress (Figure 10a) intensified the rise in η (Figure 10b) through increasing the net bay-ward transport. The correlation coefficient (CC) between the net bay-ward transport and the alongshore wind stress was ~0.84 (95% confidence interval). The rise in η occurred 1 day after the wind burst. During this process, a stretching of the vortex tube inside the bay occurred, and the anticyclonic circulation, shown in Figures 9a and 9b, was suppressed (Figure 10c). The reduction in ξ (<0) or strengthening of the anticyclonic circulation occurred 2 days after η changed, and the lag CC was ~0.82 (95% confidence interval). The coherent changes of η and ξ inside the bay indicate a general conservation of potential vorticity, which was also reported in Whitney and Allen (2009). The net intrusive current through the bay entrance weakened with the onset of a higher η in the bay (Figure 10d). The CC of the reduction in the intrusive current with the ξ variation was ~0.76 (95% confidence interval). These results confirm that the anticyclonic bay circulation was locally regulated by trough isobaths and wind forcing inside the bay and remotely controlled by the intrusive shelf current. The respective impacts of these forcings will be investigated below.

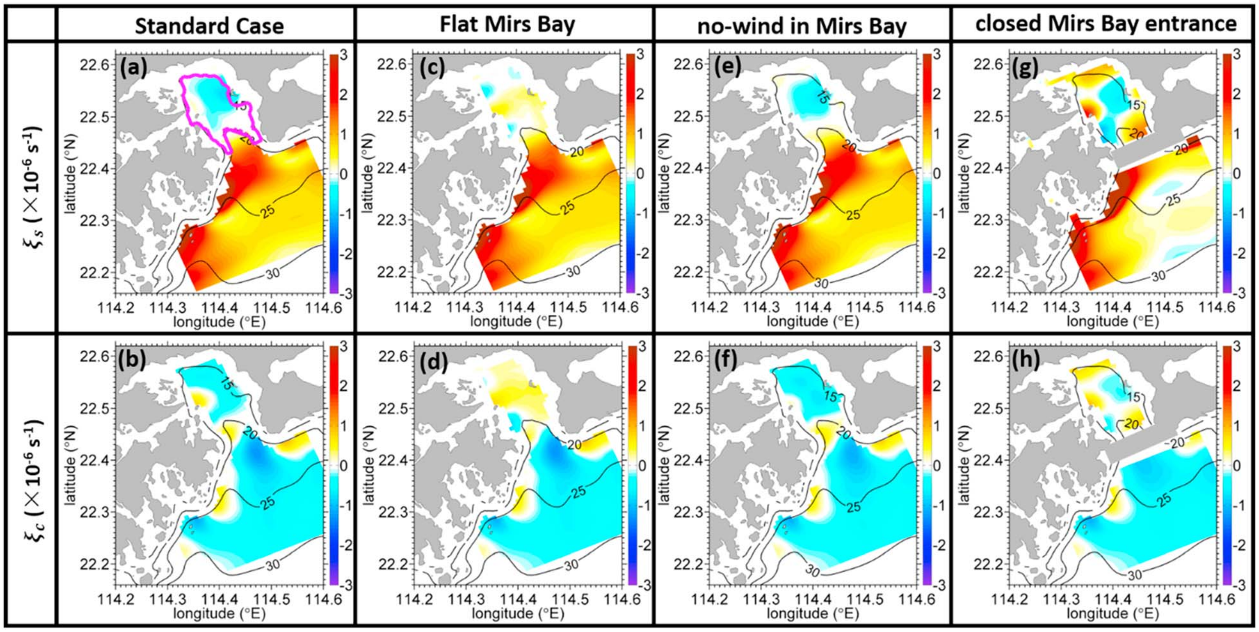

Figure 9. Horizontal distribution of depth-averaged (top) shear vorticity ($\times10^{-5}$ s^{-1}) and (bottom) curvature vorticity ($\times10^{-5}$ s^{-1}) in Mirs Bay and the neighboring shelf. The model results are averaged over the month of July 2011. (a) and (b) illustrate shear and curvature vorticity from the standard case with realistic topography and wind forcing. (c) and (d) are from the sensitivity experiment with a flattened trough inside Mirs Bay. (e) and (f) present results from the sensitivity experiment without wind forcing inside the bay, and (g) and (h) are from the sensitivity experiment with the entrance of Mirs Bay closed off. The area inside the pink line in (a) is the region where the surface elevation and relative vorticity are averaged.

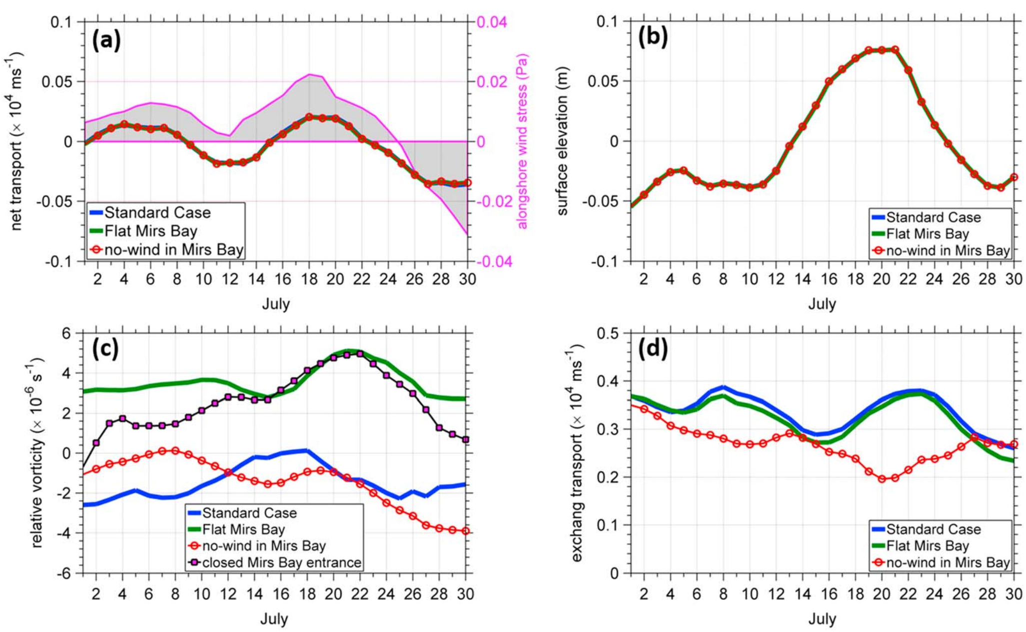

Figure 10. Time series of (a) alongshore (oriented ~22.8° east) wind stress at station MM13 in Figure 1b and net depth-integrated velocity at the bay entrance (section *Bn* in Figure 4c; a positive value indicates a bay-ward direction), (b) horizontally averaged surface elevation and (c) relative vorticity fluctuation inside the bay, and (d) depth-integrated bay-ward velocity at the bay entrance. The results presented include those from the standard case and sensitivity experiments of the flattened trough case, the windless Mirs Bay case, and the closed bay entrance case. The area used to calculate surface elevation and relative vorticity fluctuation is shown in Figure 9a.

4.2. Effects of Local Wind and Topographic Forcings

Two sensitivity experiments using the same numerical implementation as the standard case were conducted. These experiments are (1) a flat bottom inside the bay by setting the water depth as 20 m to study the role of local topography on the bay circulation; and (2) no-wind forcing inside the bay to investigate the wind effect on the bay circulation. Results from these sensitivity experiments are then compared with those from the standard case in Figures 9 and 10, and the differences in flow fields among them are demonstrated in Figure 11.

4.2.1. Topographic Forcing

Figures 9c and 9d demonstrate that, without trough isobaths inside the bay, the general bay circulation becomes cyclonic. The shelf waters are guided by the trough isobaths near the entrance and flow northeastward along the east bank of Mirs Bay (Figures 11a–11c). This cyclonic bay circulation persists throughout the study period as shown in Figure 10c. However, the time series of net transport (Figure 10a) and the time series of influx (Figure 10d) through the bay entrance, as well as the time series of η inside the bay (Figure 10b), are not different from the standard case. These findings suggest that the anticyclonic bay circulation in the standard experiment is regulated by the bay topography. The respective roles of shelf water intrusion and local wind forcing in determining the exchange flow at the bay entrance will be further investigated below.

4.2.2. Wind Forcing

The horizontal distributions of ξ_s and ξ_c (Figures 9e and 9f) and velocity vectors (Figures 11d–11f) from the second sensitivity case (no-wind forcing inside the bay) are generally consistent with those from the standard experiment (Figures 9a and 9b). This sensitivity case shows an anticyclonic bay circulation and the intrusive shelf waters flow northwestward along the west bank of the bay (Figure 11e). The fact that changes in net transport (Figure 10a) and η (Figure 10b) are similar to those in the standard case confirms that the fluctuation of η inside Mirs Bay is determined by intrusion of shelf waters along the trough inside the bay, instead of local wind forcing. The local wind forcing amplified the influx at the bay entrance (Figure 10d) and weakened ξ inside the bay (Figure 10c).

4.3. Effect of Shelf Current Intrusion

A sensitivity experiment by disconnecting the bay circulation from the intrusive current through closing the bay entrance was conducted. In addition to the properties shown in Figures 9–11, we show domain-averaged profiles of ξ, divergence of PGF ($\nabla \cdot PGF$), and its respective barotropic ($\nabla \cdot PGF_T$) and baroclinic ($\nabla \cdot PGF_C$) components, as well as potential density anomaly along section A in Figure 12 to better illustrate the buoyant effect imposed by the intrusive denser shelf waters on the circulation in the bay. $\nabla \cdot PGF_T$ and $\nabla \cdot PGF_C$ are expressed as

$$\begin{cases} \nabla\cdot PGF_T = \nabla\cdot\left(-\frac{1}{\rho_0} g\nabla\eta\right) \\ \nabla\cdot PGF_C = \nabla\cdot\left(-\frac{1}{\rho_0}\int_{-h}^{\eta} g\nabla\rho dz\right) \end{cases}, \tag{1}$$

where g is gravitational acceleration, ρ is density, and $\nabla\cdot$ is the divergence operator. It is now clear that with ξ inside Mirs Bay is 1.0–5.0 × 10^{-6} s^{-1} (Figure 9), and Coriolis parameter (f) is ~5.5 × 10^{-5} s^{-1}; Rossby number ($\frac{\xi}{f}$) is much smaller than 1.0 inside the bay, and the circulation was mainly regulated by its geostrophic component:

$$(u, v) = -\frac{1}{f\rho}\left(\frac{\partial P}{\partial y}, -\frac{\partial P}{\partial x}\right). \tag{2}$$

Thereby, under the assumption of small Rossby number, ξ can be dynamically linked to $\nabla \cdot PGF$ by substitutingthe equation (2) into $\xi = \frac{\partial u}{\partial x} - \frac{\partial y}{\partial y}$. It should also be pointed out that due to the disconnected bay and shelf circulations, the volume inside Mirs Bay is conserved with the area-averaged η = 0, and there are not influx and outflux at the entrance in Figure 10.

The horizontal distributions of ξ_s and ξ_c in Figures 9g and 9h and velocity vectors in the upper and intermediate layers (Figures 11g and 11h) show that without shelf current intrusion, the flow alternates between a

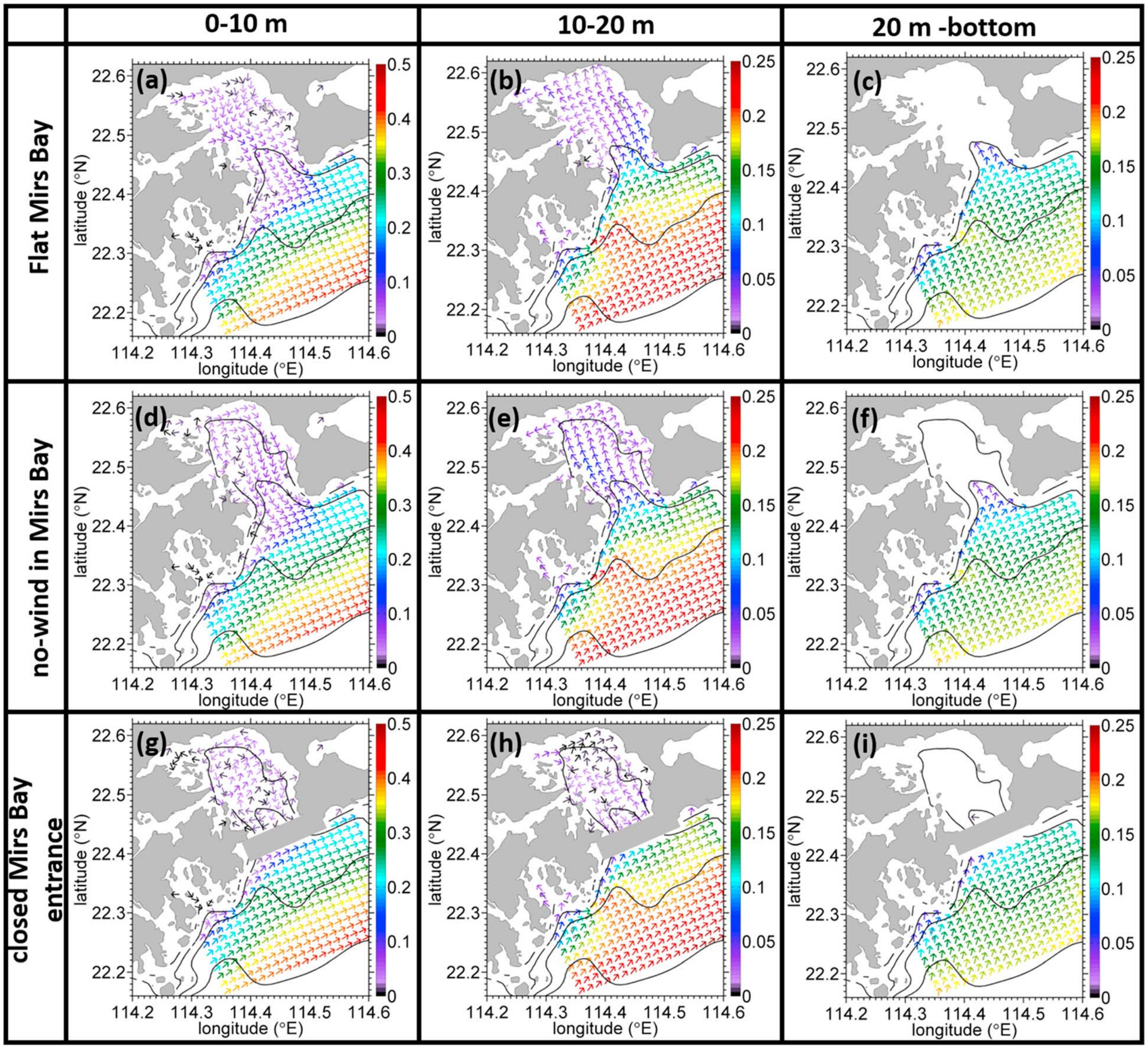

Figure 11. Similar to Figures 4a–4c but for sensitivity experiments with (a–c) a flattened trough inside Mirs Bay, (d–e) no wind forcing inside the bay, and (g–i) a closed bay entrance.

cyclonic and an anticyclonic circulation, while the averaged vorticity becomes cyclonic, as a result of local wind forcing (Figure 10c). This further indicates that the bay circulation is regulated by the intruded shelf current and the bay topography itself, instead of wind.

Figures 12a and 12b further reveal that in the water column, the circulation in the lower half of Mirs Bay showed a two-layer structure, that is, anticyclonic in the upper layer and cyclonic in the intermediate layer. This flow pattern is consistent with the vertical distribution of $\nabla \cdot PGF$, which is composed of the positive/negative contribution from $\nabla \cdot PGF_T/\nabla \cdot PGF_C$ in the standard case (Figures 12b–12d) and the sensitivity experiment (Figures 12f–12h). The intrusive shelf waters intensify both the anticyclonic circulation in the upper layer through increasing η inside the bay (Figure 10b) and the cyclonic circulation in the intermediate layer through importing denser waters and increasing stratification inside Mirs Bay (Figure 12d). Without the denser intrusive shelf water, the anticyclonic circulation in the upper layer is weakened, while the intermediate cyclonic circulation is intensified (Figure 12e) as the denser intrusive water is trapped near the bay entrance (Figure 12h).

10.1029/2018JC013830

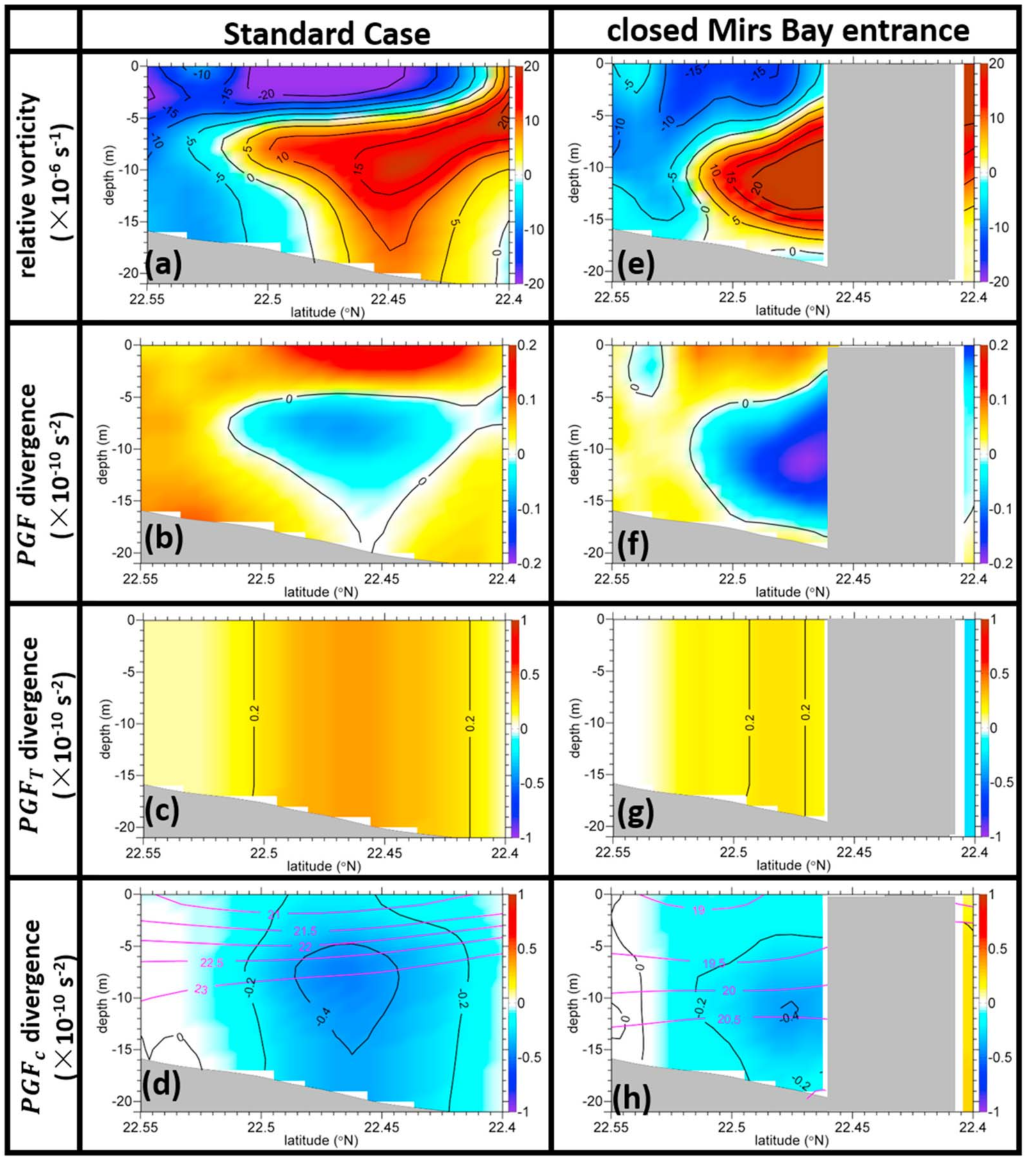

Figure 12. Transects of (a, e) relative vorticity, (b, f) $\nabla \cdot PGF$, (c, g) $\nabla \cdot PGF_T$, and (d, h) $\nabla \cdot PGF_C$ along section A in Figure 4a. The model results are from the (a–d) standard case and (e–h) sensitivity experiments of the case with a closed Mirs Bay entrance. The results are averaged over the month of July 2011. Transects of potential density anomaly for the standard case and sensitivity experiments are superimposed in (d, h) as purple contour lines.

4.4. Bay-Ward Cross-Isobath Transport Over the Shelf

Observational and modeling results showed that the intensified cross-isobath transport over the topographic trough provided the bay-ward intrusion and governed largely the bay circulation. In this section, the forcing mechanism for the cross-isobath transport is examined based on analyses of terms in a depth-averaged momentum and depth-integrated vorticity equation.

The depth-averaged along-isobath momentum (equation (3)) and depth-integrated vorticity equations (equation (4)) are used to determine the dynamics of the shelf current cross-shore intrusion. In these equations, the subscripts ($x*$, $y*$) represent the balances in the cross- and along-isobath directions, respectively. The along-isobath momentum equation (3) is composed by acceleration ($ACCEL_{y*}$), Coriolis force (COR_{y*}) due to earth rotation, horizontal nonlinear advection ($HADV_{y*}$), pressure gradient force (PGF_{y*}), wind stress ($SSTR_{y*}$), frictional bottom stress ($BSTR_{y*}$), and the horizontal viscous term ($HVISC_{y*}$). Equation (3) can be expressed as

$$\overbrace{\frac{\partial \overline{v}}{\partial t}}^{ACCEL_{y*}} = \overbrace{-f\overline{u}}^{COR_{y*}} \overbrace{-[(\overline{u},\overline{v})\cdot\nabla]\overline{v}}^{HADV_{y*}} - \overbrace{\frac{P_{y*}}{\rho_0 D}}^{PGF_{y*}} + \overbrace{\frac{\tau_{sy*}}{\rho_0 D}}^{SSTR_{y*}} - \overbrace{\frac{\tau_{by*}}{\rho_0 D}}^{BSTR_{y*}} + \overbrace{K_h \nabla^2 \overline{v}}^{HVISC_{y*}}. \tag{3}$$

The PGF_{y*} can be further decomposed by using the following depth-integrated vorticity equation (4) proposed by Gan et al. (2013). The terms in this equation are along-isobath PGF_{y*}, which is also the pressure gradient force term in the right-hand side of the equation (3), joint effect of baroclinic and relief (*JEBAR*), net stress curl of the bottom stress curl (*BSC*), surface stress curl (*SSC*), nonlinear advection of relative vorticity (*RVA*), and gradient of momentum flux (*GMF*). Equation (4) formed by these terms are

$$\overbrace{\frac{-1}{\rho_0} P_{y*}}^{PGF_{y*}} = \overbrace{\frac{1}{D_{x*}} \nabla \times \left(\frac{\frac{g}{\rho_0} \int_{-H}^{0} z\rho dz \nabla H}{H} \right)}^{JEBAR} + \overbrace{\frac{1}{D_{x*}} \overline{\nabla} \times \left(\frac{\tau_b}{\rho_0} \right)}^{BSC} + \overbrace{\frac{1}{D_{x*}} \overline{\nabla} \times \left(-\frac{\tau_s}{\rho_0} \right)}^{SSC} + \overbrace{\frac{1}{D_{x*}} J(\psi, \xi)}^{RVA} + \overbrace{\left(\frac{\left\| \vec{v} \right\|^2}{2} \right)_{y*}}^{GMF}. \tag{4}$$

The *BSC* term in equation (4) can be further decomposed into contributions from the curvature (ξ_{bc}) and shear (ξ_{bs}) vorticity by using the law of quadratic friction as

$$\overbrace{\frac{1}{D_{x*}} \overline{\nabla} \times \frac{\tau_b}{\rho_0}}^{BSC} = \overbrace{\frac{C_d}{D_{x*}} \|V_b\| \xi_{bc}}^{BSC_c} + \overbrace{\frac{2C_d}{D_{x*}} \|V_b\| \xi_{bs}}^{BSC_s}. \tag{5}$$

Thus, the ξ_{bc} and ξ_{bs} contribution to the *BSC* are expressed as BSC_c and BSC_s, as shown in equation (5).

The time series of these terms in the along-isobath direction by averaging them in the area bordered by sections *Us*, *Ds*, *Cr*, and *Bn* in Figure 4c, where extensive upwelling circulation occurred, were shown in Figures 4d–4f. The time series of terms in equations (3)–(5) are shown in Figures 13a–13c, respectively. We illustrate the monthly averaged horizontal distribution of the terms that make up the first-order balances in equations (3)–(5) in Figure 13d.

The time series of the volume-averaged momentum terms from equation (3) demonstrate the importance of the negative along-isobath PGF_{y*} over the trough for the geostrophic upslope intrusion of deep shelf water off the entrance of Mirs Bay (Figure 13a). The geostrophic cross-shore intrusion, associated with this PGF_{y*}, was remarkably stronger (~10 times) than the intrusion attributed to the surface ($SSTR_{y*}$) and bottom ($BSTR_{x*}$) Ekman transport as well as to the nonlinearity of the shelf current ($HADV_{y*}$). Contributions to this onshore intrusion from the other processes ($ACCEL_{y*}$ and $HVISC_{y*}$) were negligible. The monthly averaged horizontal distributions of this PGF_{y*} in equation (3) had a pattern similar to that in the bottom layers, on the shelf off the bay entrance (Figure 13d). The PGF_{y*} in the bottom layer is named as *PYB*. This consistency between *PYB* and PGF_{y*} suggests that *JEBAR* was insignificant.

Over the trough isobaths over the shelf, we observed that the major contributor to PGF_{y*} was *RVA*, caused by a negative ξ advection on the shelf near the concave trough, where both ξ_s and ξ_c decreased (Figures 9a and 9b) and the velocity intensified downstream of the shelf current (Figures 4a–4c and 5). The downstream decreases in ξ_s, and ξ_c occurred when the shelf current flowed over the trough (Figures 9a and 9b). The vortex tube, associated with this shelf current, was stretched at the west bank of the trough, while it was squeezed at the east bank to weaken the ξ, for example, at 114.42°E and 23.32°N. The dominant role of *RVA* can also be seen clearly from the monthly averaged horizontal distributions in Figure 13d, where a stream of negative *RVA* manifested over the trough.

SSC in equation (4) occasionally contributed to the formation of this PGF_{y*} when there was a positive wind stress curl, for example, on 14–24 July 2011. Different from what Liu and Gan (2014; 2015) reported, *BSC* was not critical in determining the formation of the negative PGF_{y*} in the study area. The positive *BSC* offsets the negative PGF_{y*} and was mainly formed by the positive ξ_s on the shore side of the coastal jet. The location

10.1029/2018JC013830

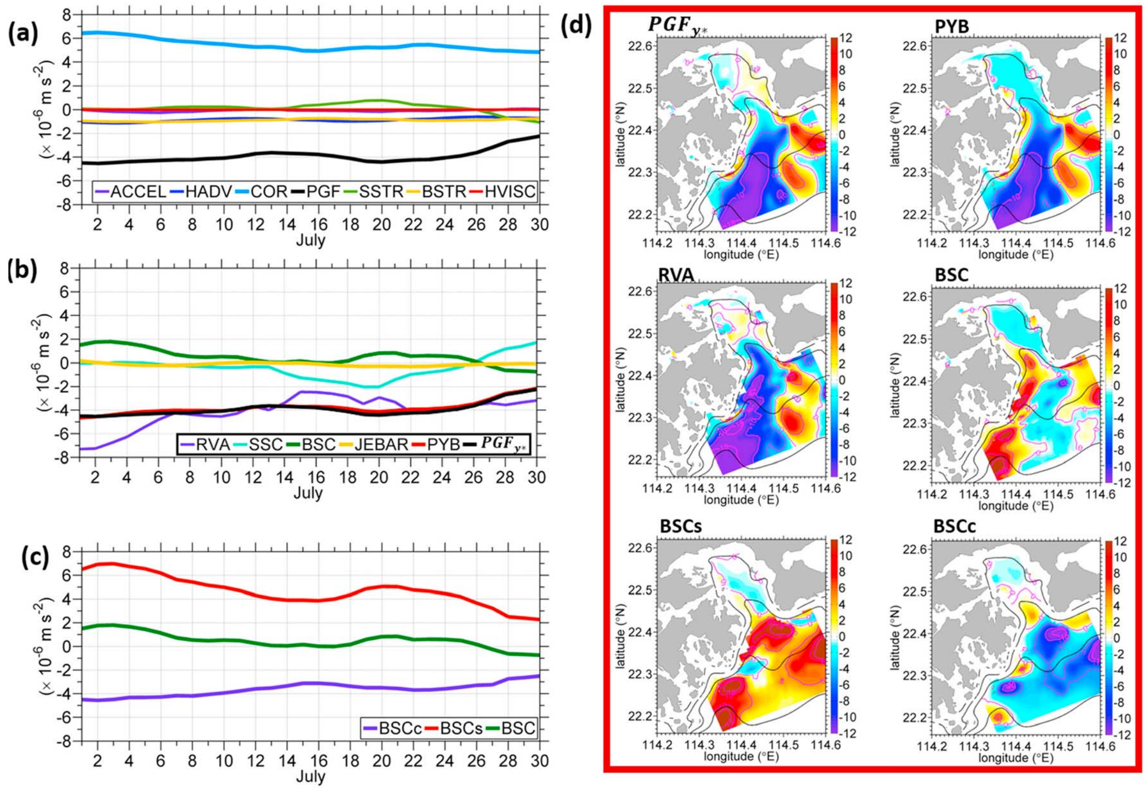

Figure 13. Time series of terms (×10^{-6} m/s^2) from (a) equation (3), (b) equation (4), and (c) equation (5). These terms are in the along-isobath direction and horizontally averaged over the shelf southeast of the bay entrance, bounded by transects *Bn*, *Us*, *Ds*, and *Cr* shown in Figure 4c. (d) Horizontal distribution of the dominant along-isobath PGF_{y*} (×10^{-6} m/s^2, first row) in the surface layer and in equation (3) and the dominant terms (×10^{-6} m/s^2, second row) in equation (4) and (×10^{-6} m s^{-2}, third row) equation (5). The horizontal distributions of the terms in (d) were averaged over the month of July 2011. ACCEL = acceleration; HADV = horizontal nonlinear advection; COR = Coriolis force; PGF = pressure gradient force; SSTR = wind stress; BSTR = frictional bottom stress; HVISC = horizontal viscous term; RVA = nonlinear advection of relative vorticity; SSC = surface stress curl; BSC = bottom stress curl; JEBAR = joint effect of baroclinic and relief; PYB = bottom layer pressure gradient force.

of the jet was largely determined by the lateral density gradient in the river plume over the shelf. Decomposing the BSC_c and BSC_s contributions (Figure 13c) following equation (5) reveals the contribution of *BSC* to PGF_{y*} and the dynamic differences between the upwelling in this study and what previous studies in the East China Sea reported (Liu & Gan, 2014). In response to the offshore positioning of the shelf current, a notable positive ξ_{bs} led to a remarkable consumption of the negative PGF_{y*} on the lee side of Hong Kong. Although there was a negative ξ_{bc}, due to the anticyclonic rotation of the shelf current, its intensity was much smaller than ξ_{bs} (Figure 13d). A positive BSC_s controlled the formation of *BSC* as shown in Figures 13c and 13d. This positive *BSC* suppressed the geostrophic onshore intrusion of shelf water.

5. Summary

The processes and dynamics governing the formation of an intensified summer upwelling circulation off Mirs Bay, Hong Kong, and its control on the circulation in the adjacent coastal bay are investigated in this research. Based on analyses of long- and short-term hydrographic observations and a validated numerical model, the underlying forcing processes of the shelf-bay coupled circulation is studied.

The shelf circulation was characterized by persistent upwelling. A surface cold-water stream extended northeastward and bypassed the entrance of Mirs Bay. The intrusion of deep shelf water into the bay, as a result of the upwelling circulation mainly occurred below 10 m. Field observations of hydrographic properties and time-series monitoring revealed the existence of a northeast bay-ward current on the lee side of Hong Kong with a two-layer exchange flow between the shelf and the bay.

A high-resolution-coupled bay-shelf-estuary numerical model was conducted to simulate observed features and to investigate the self-bay circulation. The model was coupled to a larger-scale NSCS model, and the NSCS model was subsequently nested within a China Sea model. The model results captured the observed features satisfactorily.

The northeastward flowing upwelling jet over the shelf southeast of Hong Kong showed enhanced bay-ward intrusion over the trough isobaths. The cold deep shelf waters moved shoreward, guided by the trough isobaths that protruded all the way from the shelf toward the bay and intruded into the bay. The current in the bay circulates anticyclonically, with a two-layered exchange flow over the bay's entrance. The shelf and bay circulations interacted with each other. The bay circulation tended to deter the current intrusion from the shelf due to the bay-ward pressure gradient that was setup by the anticyclonic and upwelling circulations in the bay and adjacent shelf, respectively.

Numerical experiments identified the relative importance of local topography, wind forcing, and remote shelf current intrusion for the coupled shelf-bay circulation. The anticyclonic bay circulation was regulated by the intruding shelf current over the bay topography. Wind increased the exchange flow at the bay entrance but imposed a positive vorticity to offset the anticyclonic bay circulation. Without intrusion from the upwelling circulation over the shelf, the wind-driven circulation in the bay would be cyclonic. In addition, the intrusion of denser shelf waters baroclinically modulated the pressure gradient field in the anticyclonic circulation in the bay.

The strengthened intrusive deep shelf water over trough isobaths, which was critical to the formation of the anticyclonic circulation in the bay, was induced by the intensified southwestward along-isobath pressure gradient force over the isobaths. The origin of this pressure gradient force was the negative relative vorticity advection due to the decreased relative vorticity and the intensified upwelling jet to the downstream of the bay entrance.

Acknowledgments
The work was supported by the Theme-based Research Scheme (T21-602/16-R) of the Hong Kong Research Grants Council and by the Seed Collaborative Research Fund of the State Key Laboratory in Marine Pollution (SKLMP). We are grateful to National Supercomputer Center of Tianhe-1 (Tianjin) and Tianhe-2 (Guangzhou). The data used in this study were derived from public data set and from field measurement, and they are all included as supporting information to this paper. The model data for this study are produced by community model ROMS (https://www.myroms.org/). Observational data are included as supporting information. The authors are grateful for the thoughtful comments and suggestions from the anonymous reviewers.

References

Carballo, R., Iglesias, G., & Castro, A. (2009). Residual circulation in the Ria de Muros (NW Spain): A 3D numerical model study. *Journal of Marine Systems*, *75*(1–2), 116–130. https://doi.org/10.1016/j.jmarsys.2008.08.004

Chau, Y., & Abesser, R. (1958). A preliminary study of the hydrology of Hong Kong territorial waters. *Hong Kong University Fisheries Journal*, *2*, 43–58.

Egbert, G. D., & Erofeeva, S. Y. (2002). Efficient inverse modeling of barotropic ocean tides. *Journal of Atmospheric and Oceanic Technology*, *19*(2), 183–204. https://doi.org/10.1175/1520-0426(2002)019<0183:EIMOBO>2.0.CO;2

Flather, R. A. (1976). A tidal model of the northwest European continental shelf. *Memoires de la Societe Royale des Sciences de Liege*, *10*, 141–164.

Gan, J. P., & Allen, J. S. (2002). A modeling study of shelf circulation off northern California in the region of the Coastal Ocean Dynamics Experiment: Response to relaxation of upwelling winds. *Journal of Geophysical Research*, *107*(C9), 3123. https://doi.org/10.1029/2000JC000768

Gan, J. P., & Allen, J. S. (2005). On open boundary conditions for a limited-area coastal model off Oregon. Part 1: Response to idealized wind forcing. *Ocean Modelling*, *8*(1-2), 115–133. https://doi.org/10.1016/j.ocemod.2003.12.006

Gan, J. P., Ho, H. S., & Liang, L. L. (2013). Dynamics of intensified downwelling circulation over a widened shelf in the northeastern South China Sea. *Journal of Physical Oceanography*, *43*(1), 80–94. https://doi.org/10.1175/JPO-D-12-02.1

Gan, J. P., Liu, Z. Q., & Liang, L. L. (2016). Numerical modeling of intrinsically and extrinsically forced seasonal circulation in the China Seas: A kinematic study. *Journal of Geophysical Research: Oceans*, *121*, 6184–6203. https://doi.org/10.1002/2016JC011975

Gan, J. P. A., Cheung, X. G. G., & Li, L. (2009). Intensified upwelling over a widened shelf in the northeastern South China Sea. *Journal of Geophysical Research*, *114*, C09019. https://doi.org/10.1029/2007JC004660

Gan, J. P. J. J. W., Liang, L. L., Li, L., & Guo, X. G. (2015). A modeling study of the formation, maintenance, and relaxation of upwelling circulation on the northeastern South China Sea shelf. *Deep Sea Research Part II*, *117*, 41–52. https://doi.org/10.1016/j.dsr2.2013.12.009

Gan, J. P., Li, L., Wang, D. X., & Guo, X. G. (2009). Interaction of a river plume with coastal upwelling in the northeastern South China Sea. *Continental Shelf Research*, *29*(4), 728–740. https://doi.org/10.1016/j.csr.2008.12.002

Klinck, J. M., Obrien, J. J., & Svendsen, H. (1981). A simple-model of fjord and coastal circulation interaction. *Journal of Physical Oceanography*, *11*(12), 1612–1626. https://doi.org/10.1175/1520-0485(1981)011<1612:ASMOFA>2.0.CO;2

Large, W. G., & Pond, S. (1981). Open ocean momentum flux measurements in moderate to strong winds. *Journal of Physical Oceanography*, *11*(3), 324–336. https://doi.org/10.1175/1520-0485(1981)011<0324:OOMFMI>2.0.CO;2

Lee, J. H., Harrison, P. J., Kuang, C., & Yin, K. (2006). Eutrophication dynamics in Hong Kong coastal waters: Physical and biological interactions. In *The environment in Asia Pacific harbours* (pp. 187–206). Dordrecht, Netherands: Springer. https://doi.org/10.1007/1-4020-3655-8_13

Liu, Z., & Gan, J. (2014). Modeling study of variable upwelling circulation in the East China Sea: Response to a coastal promontory. *Journal of Physical Oceanography*, *44*, 1078–1094. https://doi.org/10.1175/JPO-D-13-0170

Liu, Z., & Gan, J. (2015). Upwelling induced by the frictional stress curl and vertical squeezing of the vortex tube over a submerged valley in the East China Sea. *Journal of Geophysical Research: Oceans*, *120*, 2571–2587. https://doi.org/10.1002/2015JC010715

Mellor, G. L., & Yamada, T. (1982). Development of a turbulence closure-model for geophysical fluid problems. *Reviews of Geophysics*, *20*(4), 851–875. https://doi.org/10.1029/RG020i004p00851

Moraga-Opazo, J., Valle-Levinson, A., Ramos, M., & Pizarro-Koch, M. (2011). Upwelling-triggered near-geostrophic recirculation in an equatorward facing embayment. *Continental Shelf Research*, *31*(19-20), 1991–1999. https://doi.org/10.1016/j.csr.2011.10.002
Shchepetkin, A. F., & McWilliams, J. C. (2005). The Regional Oceanic Modeling System (ROMS): A split-explicit, free-surface, topography-following-coordinate oceanic model. *Ocean Modelling*, *9*(4), 347–404. https://doi.org/10.1016/j.ocemod.2004.08.002
Song, Y. T., & Haidvogel, D. B. (1994). A semi-implicit ocean circulation model using a generalized topography-following coordinate system. *Journal of Computational Physics*, *115*(1), 228–244. https://doi.org/10.1006/jcph.1994.1189
Song, Y. T., Haidvogel, D. B., & Glenn, S. M. (2001). Effects of topographic variability on the formation of upwelling centers off New Jersey: A theoretical model. *Journal of Geophysical Research*, *106*(C5), 9223–9240. https://doi.org/10.1029/2000JC000244
Souto, C., Gilcoto, M., Farina-Busto, L., & Perez, F. F. (2003). Modeling the residual circulation of a coastal embayment affected by wind-driven upwelling: Circulation of the Ria de Vigo (NW Spain). *Journal of Geophysical Research*, *108*(C11), 3340. https://doi.org/10.1029/2002JC001512
Tee, K. T., Smith, P. C., & Lefaivre, D. (1993). Topographic upwelling off Southwest Nova Scotia. *Journal of Physical Oceanography*, *23*(8), 1703–1726. https://doi.org/10.1175/1520-0485(1993)023<1703:TUOSNS>2.0.CO;2
Wang, D.-P., & Elliott, A. J. (1978). Non-tidal variability in the Chesapeake Bay and Potomac River: Evidence for non-local forcing. *Journal of Physical Oceanography*, *8*(2), 225–232. https://doi.org/10.1175/1520-0485(1978)008<0225:NTVITC>2.0.CO;2
Weisberg, R. H., Black, B. D., & Li, Z. J. (2000). An upwelling case study on Florida's west coast. *Journal of Geophysical Research*, *105*(C5), 11,459–11,469. https://doi.org/10.1029/2000JC900006
Whitney, M. M., & Allen, J. S. (2009). Coastal wind-driven circulation in the vicinity of a bank. Part I: Modeling flow over idealized symmetric banks. *Journal of Physical Oceanography*, *39*(6), 1273–1297. https://doi.org/10.1175/2008JPO3966.1
Wong, K. C., & Garvine, R. W. (1984). Observations of wind-induced, subtidal variability in the Delaware Estuary. *Journal of Geophysical Research*, *89*, 589–597.
Yin, K. D. (2002). Monsoonal influence on seasonal variations in nutrients and phytoplankton biomass in coastal waters of Hong Kong in the vicinity of the Pearl River Estuary. *Marine Ecology Progress Series*, *245*, 111–122. https://doi.org/10.3354/meps245111
Zu, T. T., & Gan, J. P. (2015). A numerical study of coupled estuary-shelf circulation around the Pearl River Estuary during summer: Responses to variable winds, tides and river discharge. *Deep Sea Research Part II*, *117*, 53–64. https://doi.org/10.1016/j.dsr2.2013.12.010
Zu, T. T., Gan, J. P., & Erofeeva, S. Y. (2008). Numerical study of the tide and tidal dynamics in the South China Sea. *Deep Sea Research Part I*, *55*(2), 137–154. https://doi.org/10.1016/j.dsr.2007.10.007